frontiers | Frontiers in Physics

TYPE Original Research
PUBLISHED 12 April 2023
DOI 10.3389/fphy.2023.1126003

OPEN ACCESS

EDITED BY
Stefano Leonardi,
The University of Texas at Dallas,
United States

REVIEWED BY
Mustafa Turkyilmazoglu,
Hacettepe University, Türkiye
B. Rushi Kumar,
VIT University, India

*CORRESPONDENCE
Adriana Cătaş,
acatas@gmail.com

†These authors have contributed equally to this work

SPECIALTY SECTION
This article was submitted to Fluid Dynamics, a section of the journal Frontiers in Physics

RECEIVED 16 December 2022
ACCEPTED 15 March 2023
PUBLISHED 12 April 2023

CITATION
Sanni KM, Asghar S, Al-Shbeil I and Cătaş A (2023), Radiative simulation of non-Newtonian MHD fluid over a boundary-driven multi-physical curved mechanism: Keller–Box evidence. *Front. Phys.* 11:1126003. doi: 10.3389/fphy.2023.1126003

Radiative simulation of non-Newtonian MHD fluid over a boundary-driven multi-physical curved mechanism: Keller–Box evidence

Kehinde M. Sanni[1†], Saleem Asghar[2†], Isra Al-Shbeil[3†] and Adriana Cătaş[4*†]

[1]Department of Mathematics, Chak Shahzad, COMSATS University, Islamabad, Pakistan, [2]Department of Mathematics, COMSATS University Islamabad, Islamabad, Pakistan, [3]Department of Mathematics, Faculty of Science, The University of Jordan, Amman, Jordan, [4]Department of Mathematics and Computer Science, University of Oradea, Oradea, Romania

This study is numerically driven to ascertain the flow of two-dimensional heat transfer of an incompressible electrically conducting non-Newtonian fluid over a continuous power-law stretching curved surface. The flow model considers rheological fluid viscosity using curvilinear (r –, s –) coordinates. The energy equation for the curved mechanism is examined in two streams: the prescribed surface temperature and the prescribed heat flux. Surface frictional heating is influenced by thermal radiation and viscous dissipation. Similarity transformations are executed to reduce partial differential equations into ordinary differential equations. The Keller–Box shooting method with the Jacobi iterative techniques is numerically computed for the degenerated nonlinear system of the boundary value problem. The associated boundary-layer thickness and flow fields- velocity and temperature are analyzed against characterizing parameters. Significant results are obtained and discussed with graphical plots showing that fluid velocity can be controlled by virtue of fluid parameters and stretching power index. These results are useful in polymer dynamics involving the melting and manufacturing of stretchable sheets.

KEYWORDS

nonlinear, MHD, curved sheet, radiation, viscous dissipation, power-law, Keller-Box, error analysis

1 Introduction

The heat transfer analysis for non-Newtonian fluid flow driven by a nonlinear boundary surface has received great attention for decades. Most fluids found in science, engineering, and manufacturing industry, such as biological fluids, foodstuff, cosmetics and toiletries, particulate slurries, multi-phase fluid mixtures, synthetic lubricants, paints, and numerous polymeric

Abbreviations: η_0, zero viscous limit; η_∞, infinite viscous limit; m, fluid behavioral index; $\triangle$, dynamic viscosity; ρ, fluid density; R, radius of curvature; σ, fluid electrical conductivity; B, magnetic field; B_0, applied magnetic field strength; (v, u), velocity in radial and axial directions; H_a, Hartmann number; β_0, Sutterby fluid parameter; ξ, dimensionless curvature parameter; K_0, fluid thermal conductivity; C_p, fluid specific heat capacity; $\theta(\eta)$, dimensionless temperature for PST; $\vartheta(\eta)$, dimensionless temperature for PHF.

fluids, display characteristics that do not obey classical Newton's law of viscosity. In other words, the complex behavior of these fluids is evidenced by normal stresses, viscosity, and time-dependent elastic effect, which can be traced to being a non-Newtonian fluid. Without a unique general model to exhibit all the properties of various non-Newtonian fluids, many rheology viscous models have been proposed to capture the dynamic phenomena for the completeness of flow studies in fluid mechanics. The simplest non-Newtonian fluid model is documented as Ostwald–de Waele fluid (known as power-law fluid), which explains the occurrence of a real non-Newtonian fluid. It classifies non-Newtonian fluids as shear thinning ($n < 1$) and shear thickening ($n > 1$) with the limitation of not being able to predict the stress relaxation time and elasticity performance of viscoelastic fluids. The second-, third-, and fourth-grade fluids are subclasses of differential-type materials that can predict normal stress, shear thinning, and shear thickening but do not capture time-dependent relaxation. A linear viscoelastic (Maxwell fluid) model is characterized by relaxation time and explains the properties of polymeric fluids but fails in cognizance of the shear thinning and thickening properties of the fluids. Other non-Newtonian fluids, including Jeffrey fluid, Williamson fluid, Casson fluid, Reiner–Philipoff fluid, Ellis fluid, Eyring viscous fluid, Power–Eyring fluid, Prandtl–Erying fluid, Sisco fluid, Carreau fluid, Nanofluid, and Meter, are characterized by shearing stress, implicit and explicit expression of strain rate, and composite function of strain rate [1–8]. The study of non-Newtonian fluids and heat transfer has numerous applications in engineering productions and the polymer industry. It enhances the quality of the finished product through heating and cooling processes. Some recent studies in this direction include a stagnation stretching sheet for a flow of Maxwell fluid in the presence of radiative heat flux analyzed by [9]. Jawadi et al. [10] investigated the asymptotic power-law fluid flow with a numerical technique for the unsteady scenario. The Rayleigh–Stokes problem with the energy balance of a Maxwell fluid is studied by [11]. Hayat et al. [12] analyzed the flow of MHD Cross fluid with heat transfer over a stretching sheet through numerical computations. Ijaz et al. [13] considered the numerical simulation of MHD Cross fluid flow over a point-stagnation stretched sheet with heat transfer. Manzur et al. [14] examined the flow of Cross fluid influenced by thermal radiation with mixed convective boundary conditions and buoyancy effects. Khan et al. [15] presented an axisymmetric flow of Cross fluid over a radially varying stretching plate in the presence of heat transfer phenomena. For more studies, readers can visit [16–22]; [23]. Recently, the non-Newtonian viscous model given by Sutterby [24] has attracted the keen interest of researchers to capture some limitations witnessed in non-Newtonian fluids. For example, the power-law (Ostwald–de Waele) model, which cannot describe zero and high viscous shear rates (i.e., η_0 and η_∞, respectively), only applies to the intermediate shear rate. The Ellis model covers the zero shear rate η_0 and cannot account for the infinite shear rate η_∞. The Power–Erying and Seely models need to be amended to fit viscosity data on the entire range of shear rates. Furthermore, the Meter and Ellis models may not have reproduced Newtonian fluid in the limit case without meeting certain conditions. However, the Sutterby fluid model returns to the Newtonian fluid when $m = 0$, reduces to Erying fluid if $\eta_\infty = 0$, and Erying–Power fluid as $\eta_\infty \neq 0$ with significant flexibility of curve fitting parameters. It is noted that the infinite shear rate is not seen as a limitation due to rare practical occurrences in an industrial situation. Gangadhar et al. [25] considered the numerical Keller–Box simulation of thermo-diffusion effects on the MHD flow of Casson fluid past a non-flatness stretching surface. The Sutterby fluid flow over a helical channel is documented by [26]. Hayat et al. [27] examined the heat transfer of a Sutterby fluid flow using a rotating disc with chemically reactive species. A numerical solution of the point stagnation flow of the Sutterby fluid in the presence of the Cattaneo–Christov heat flux model is discussed by [28]. Other relevant studies can be found [29–32]. In the last decade, attention has been given to boundary-driven flow by a curved stretching sheet. Starting from the fundamental studies in [33], [34], where viscous fluid over curved stretching sheets is investigated, these studies showed that the pressure distribution inside the boundary-layer region could not be neglected compared to the flat sheet. For more related and recent studies, readers should visit [35–39], Hayat et al. [40], and [41,42]. In the aforementioned literature, to the best of our knowledge, no consideration has been given to the heat transfer analysis of the Sutterby fluid over a curved stretching sheet. The prime motive of this work is to fill this gap for the completeness of fluid flow and examine the non-Newtonian fluid using curvilinear geometry. However, the Sutterby fluid viscosity is a generalized model that yields shear thinning fluid for $m < 0$, shear thickening fluid for $m > 0$, and a Newtonian fluid when $m = 0$. Therefore, the heat transfer of a magnetohydrodynamic Sutterby fluid past a continuous curved stretched moving surface is investigated in this study. The features of the heat flow are parameterized to prescribe surface temperature, PST, heat flux, and PHF. The flow situations are induced by radiation, viscous dissipation, and frictional heating from the surface mechanism. Evidence of the Keller–Box method enhanced with the Jacobi iterative techniques is numerically implemented. Error analysis is provided to ascertain the convergence of the scheme (see Supplementary Appendix SA1). The velocity field results show that fluid flow can be controlled by virtue of fluid parameters and stretching power index. These observations have profound applications for the flow of the polymer solution and polymer dynamics involving melting and manufacturing of stretchable mechanisms.

2 Basic model

The fundamental equation of the viscosity model is considered as follows [24]:

$$\mathbf{S} = \eta_\infty + (\eta_0 - \eta_\infty)\left[\frac{\sinh^{-1}(\alpha\Delta)}{\alpha\Delta}\right]^m \mathbf{A_1}, \tag{1}$$

where m, α, Δ, η_0, η_∞, and $\mathbf{A}_1$ represent the constant index, characteristic time, dynamic viscosity, zero and infinite viscous limit, and first Rivlin–Erickson tensor, respectively. It is worth stating that practically, η does not approach infinity in the form (η_∞) but at an extremely high shear rate. In neglecting this, Eq. 1 reduces to

$$\mathbf{S} = \eta_0\left[\frac{\sinh^{-1}(\alpha\Delta)}{\alpha\Delta}\right]^m \mathbf{A_1}, \tag{2}$$

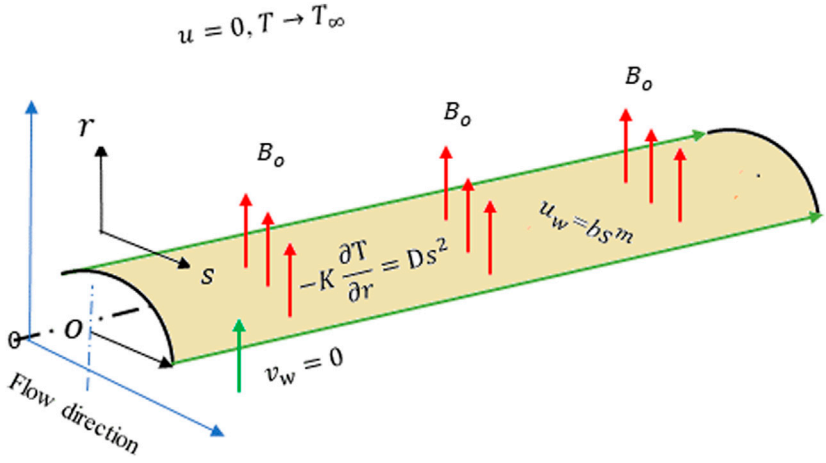

FIGURE 1
Geometry of the physical problem.

such that $\Delta = \sqrt{trace(\mathbf{A_1})^2/2}$ is the symmetry rate of deformation taking in curvilinear geometry (r-,s-). Using Navier–Stokes equation given by

$$\rho\frac{D\bar{v}}{Dt} = -\bar{\nabla}P + (\bar{\nabla}.\mathbf{S}) + \bar{\mathrm{F}}, \tag{3}$$

where D/Dt defines the time derivative, ρ is the density of the Sutterby fluid, P represents the pressure, $\bar{F}$ gives the body force, and $\bar{\nabla} = \hat{e}_r\partial_r + \lambda\hat{e}_s\partial_s$ for which $\hat{e}_r$ and $\hat{e}_s$ are orthogonal radial and axial unit vectors. Using Eqs 2, 3, the steady flow momentum equations can be expressed as

$$\begin{aligned} v\partial_r v + \lambda\partial_s v - \frac{\lambda}{R}u^2 = {} & -\frac{1}{\rho}\partial_r P + (2S_{rr} + S_{sr})\partial_r\left(\frac{\eta_0}{2}\left[\frac{\sinh^{-1}(\alpha\Delta)}{\alpha\Delta}\right]^m\right), \\ & + \left[\frac{\sinh^{-1}(\alpha\Delta)}{\alpha\Delta}\right]^m\left(\partial_r S_{rr} + \frac{\lambda S_{rr}}{R} + \lambda\partial_s S_{sr} - \frac{\lambda S_{ss}}{R}\right), \\ & + \bar{\mathbf{F}} \end{aligned} \tag{4}$$

$$\begin{aligned} v\partial_r u + \lambda\partial_s u + \frac{\lambda}{R}uv = {} & -\frac{\lambda}{\rho}\partial_s P + (S_{rs} + 2S_{ss})\lambda\partial_s\left(\frac{\eta_0}{2}\left[\frac{\sinh^{-1}(\alpha\Delta)}{\alpha\Delta}\right]^m\right), \\ & + \left[\frac{\sinh^{-1}(\alpha\Delta)}{\alpha\Delta}\right]^m\left(\lambda\partial_r S_{rs} + \frac{\lambda S_{rs}}{r+R} + \lambda^2\partial_s S_{ss} + \frac{\lambda S_{sr}}{r+R}\right), \\ & + \bar{\mathbf{F}} \end{aligned} \tag{5}$$

where η_0 is the viscosity of the Sutterby fluid, and stress components are given as $S_{rr} = \partial_r v$, $S_{rs} = S_{sr} = \partial_r u + \lambda\partial_s v - \frac{\lambda}{R}u$, $S_{ss} = \lambda\partial_r u + \frac{\lambda}{R}v$, and $\lambda = \frac{R}{r+R}$.

3 Problem description

Consider the steady flow of an electrically conducting Sutterby fluid past a power-law boundary-driven curved surface of radius R. The applied magnetic field $\bar{B}(r) = \frac{RB_0}{r+R}\hat{e}_r$ acts upwardly perpendicular to the direction of the fluid flow. The current density $J = \sigma(V \times \bar{B})$, and neglecting the electric field effect ($E \approx 0$), the Lorentz force $\bar{F} = J \times \bar{B}$ can be expressed as

$$\bar{\mathbf{F}} = \left(-\sigma\frac{\mathrm{RB_0}}{\mathrm{r+R}}\mathrm{u}, 0, 0\right), \tag{6}$$

such that σ is the electrical conductivity of the fluid and $\mathbf{B}_0$ is the strength of the applied magnetic field. The velocity vector $V = (v, u, 0)$ gives corresponding velocities v and u in the $r-$ and $s-$ directions. The physical flow geometry is shown in Figure 1.Eqs 4, 5, 6 and the continuity equation yield the following:

$$\frac{R\partial_s u}{r+R} + \frac{v}{r+R} + \partial_r v = 0, \tag{7}$$

$$\begin{aligned} v\partial_r v + \frac{R\partial_s v}{r+R} - \frac{u^2}{r+R} = {} & -\frac{\partial_r P}{\rho}, \\ & - N_1\left[4S_{rr}\partial_{rr}v + 2S_{rs}\left(\partial_{rr}u + \frac{R\partial_{rs}v}{r+R} - \frac{R\partial_s v}{(r+R)^2}\right)\right], \\ & - N_1\left[4S_{ss}\left(\frac{R\partial_{rs}u}{r+R} - \frac{R\partial_s u}{(r+R)^2} + \frac{\partial_r v}{r+R} - \frac{v}{(r+R)^2}\right)\right], \\ & + N_1\left[2S_{rs}\left(\frac{\partial_r u}{r+R} - \frac{u}{(r+R)^2}\right)\right], \\ & - N_2\left[4\frac{R\partial_r v\partial_{rs}v}{r+R} + 2\frac{RS_{rs}\partial_s(S_{rs})}{r+R} + 4\frac{RS_{ss}\partial_s(S_{ss})}{r+R}\right], \\ & + \frac{\eta_0 N_3}{\rho}\left[\frac{\partial_r[(r+R)S_{rr}]}{r+R} + \frac{R\partial_s S_{rs}}{r+R} - \frac{S_{ss}}{r+R}\right], \end{aligned} \tag{8}$$

$$\begin{aligned} v\partial_r u + \frac{R\partial_s u}{r+R} + \frac{uv}{r+R} = {} & -\frac{R\partial_s P}{\rho(r+R)}, \\ & - N_2\left[4S_{rr}\partial_{rr}v + 2S_{rs}\left(\partial_{rr}u + \frac{R\partial_{rs}v}{r+R} - \frac{R\partial_s v}{(r+R)^2}\right)\right], \\ & - N_2\left[4S_{ss}\left(\frac{R\partial_{rs}u}{r+R} - \frac{R\partial_s u}{(r+R)^2} + \frac{\partial_r v}{r+R} - \frac{v}{(r+R)^2}\right)\right], \\ & + N_2\left[2S_{rs}\left(\frac{\partial_r u}{r+R} - \frac{u}{(r+R)^2}\right)\right] - \frac{\sigma R^2 B_0^2 u}{\rho(r+R)^2}, \\ & - N_2\left[4\frac{R\partial_r v\partial_{rs}v}{r+R} + 2\frac{RS_{rs}\partial_s(S_{rs})}{r+R} + 4\frac{RS_{ss}\partial_s(S_{rs})}{r+R}\right], \\ & + \frac{\eta_0 N_3}{\rho}\left[\frac{\partial_r[(r+R)S_{sr}]}{r+R} + \frac{R\partial_s S_{ss}}{r+R} + \frac{S_{sr}}{r+R}\right], \end{aligned} \tag{9}$$

where $N_1 = \frac{m\eta_0\alpha^2 S_{rr}}{6\rho}$, $N_2 = \frac{m\eta_0\alpha^2 S_{rs}}{6\rho}$, and $N_3 = (2S_{rr}^2 + S_{rs}^2 + 2S_{ss}^2)(1 - \frac{m\alpha^2}{6})$.

Impose boundary conditions relevant to this problem as

$$u_w|_{r=0} = bs^n, v_w|_{r=0} = 0, \tag{10}$$

$$u|_{r\to\infty} = 0, \partial_r u|_{r\to\infty} = 0, \tag{11}$$

such that b ($t^{-1}l^{1-n}$) is a constant and u_w and v_w are velocities at the surface of the curved sheet. By preserving the flow properties with appropriate scaling, the non-dimensional variables are defined as

$$\bar{u} = \frac{u}{U_\infty}, \bar{v} = \frac{vl}{U_\infty \delta}, \bar{s} = \frac{s}{l}, \bar{r} = \frac{r}{\delta}, \bar{R} = \frac{R}{\delta}, \bar{P} = \frac{P}{\rho u_w^2}, \eta_1 = \frac{\eta_0 U_\infty l m \alpha^2}{6\delta^2}. \tag{12}$$

After using Eq. 12, Eqs 7–9 reduce to the boundary-layer equations:

$$\frac{R}{r+R}u^2 = \partial_r P, \tag{13}$$

$$\begin{aligned} v\partial_r u + \frac{R}{r+R}\partial_s u + \frac{uv}{r+R} = & -\frac{R}{r+R}\partial_s P, \\ & + N_4\left(3\partial_{rr}u - \frac{\partial_r u}{r+R} + \frac{u}{(r+R)^2}\right), \\ & + \frac{\eta_0}{\rho}\left(\partial_{rr}u + \frac{\partial_r u}{r+R} - \frac{u}{(r+R)^2}\right), \\ & - \frac{\sigma R^2 B_0^2 u}{\rho(r+R)^2}, \end{aligned} \tag{14}$$

where $N_4 = \eta_1\left(\partial_r u - \frac{u}{r+R}\right)^2$ and the continuity equation is identically satisfied.

The similarity variables are introduced in the following form:

$$\eta = \frac{r}{\delta}, \xi = \frac{R}{\delta}, u_w = bs^n f'(\eta), P = b^2 s^2 P^\star, \tag{15}$$

$$\delta = s\sqrt{\frac{\nu}{bs^{(n+1)}}}, H_0 = \sqrt{\frac{\sigma B_0^2 b^2}{\eta_0}}, Re_s^{\frac{1}{2}} = \sqrt{\frac{bs^{(n+1)}}{\nu}}, \tag{16}$$

$$v = -\frac{bRs^n}{r+R}\sqrt{\frac{\nu}{bs^{(n+1)}}}\left[\left(\frac{n+1}{2}\right)\frac{df}{d\eta} + \eta\left(\frac{n-1}{2}\right)\frac{df}{d\eta}\right], \tag{17}$$

where $f(\eta)$ represents the stream function, whereas the primes denote the derivative with respect to η. Using Eqs 15–17 in Eqs 13, 14, one can get the following:

$$\frac{1}{\eta+\xi}\left(\frac{df}{d\eta}\right)^2 = \frac{dP^*(\eta)}{d\eta}, \tag{18}$$

$$\begin{aligned} \frac{2n\xi}{\eta+\xi}P^* + \frac{\eta\xi}{\eta+\xi}\left(\frac{n-1}{2}\right)\frac{dP^*(\eta)}{d\eta} - \frac{d^3f}{d\eta^3} - \frac{1}{(\eta+\xi)}\frac{d^2f}{d\eta^2} + \frac{1}{(\eta+\xi)^2}\frac{df}{d\eta}, \\ = \frac{\xi}{\eta+\xi}\left[\left(\frac{n+1}{2}\right)f\frac{d^2f}{d\eta^2} - n\left(\frac{df}{d\eta}\right)^2\right] - \frac{H_0^2\xi^2}{(\eta+\xi)^2}\frac{df}{d\eta}, \\ - m\beta_0\left(\frac{d^2f}{d\eta^2} - \frac{1}{(\eta+\xi)}\frac{df}{d\eta}\right)^2\left(3\frac{d^3f}{d\eta^3} - \frac{1}{(\eta+\xi)}\frac{df^2}{d\eta^2} + \frac{1}{(\eta+\xi)^2}\frac{df}{d\eta}\right), \\ + \frac{\xi}{(\eta+\xi)^2}\left[\left(\frac{n+1}{2}\right)f\frac{df}{d\eta} + \eta\left(\frac{n-1}{2}\right)\left(\frac{df}{d\eta}\right)^2\right], \end{aligned} \tag{19}$$

such that H_0 and $\beta_0 = \frac{mb^4\alpha^2}{6}$ represent the Hartmann number and Sutterby fluid parameter, respectively. Equation 19 in limiting scenario as $\xi \to \infty$ and $P^* = 0$ yields a generalized Sutterby fluid model over a flat surface:

$$m\beta_0\left(\frac{d^2f}{d\eta^2}\right)^2\frac{d^3f}{d\eta^3} = \frac{d^3f}{d\eta^3} + \left(\frac{n+1}{2}\right)f\frac{d^2f}{d\eta^2} - n\left(\frac{df}{d\eta}\right)^2 - H_0^2\frac{df}{d\eta}. \tag{20}$$

This equation confirms the present physical models. Numerical solutions have been provided for the Newtonian fluid case, $\beta_0 = 0$, and the non-Newtonian case, $\beta_0 > 0$, over a flat stretching sheet [1,5].

Removing the pressure term, after incorporating Eq. 18, Eq. 19 gives

$$\begin{aligned} \frac{d^4f}{d\eta^4} + \frac{2}{(\eta+\xi)}\frac{d^3f}{d\eta^3} + \frac{1}{(\eta+\xi)^3}\frac{df}{d\eta} + \frac{\xi}{\eta+\xi}\left[\left(\frac{n+1}{2}\right)f\frac{d^3f}{d\eta^3} - \left(\frac{3n-1}{2}\right)\frac{df}{d\eta}\frac{d^2f}{d\eta^2}\right], \\ - \frac{1}{(\eta+\xi)^2}\frac{d^2f}{d\eta^2} + \frac{\xi}{(\eta+\xi)^2}\left[\left(\frac{n+1}{2}\right)f\frac{d^2f}{d\eta^2} - \left(\frac{3n-1}{2}\right)\left(\frac{df}{d\eta}\right)^2\right], \\ - N_5\left[3\frac{d^2f}{d\eta^2}\frac{d^4f}{d\eta^4} - \frac{3}{\eta+\xi}\frac{df}{d\eta}\frac{d^4f}{d\eta^4} - \frac{2}{\eta+\xi}\frac{d^2f}{d\eta^2}\frac{d^3f}{d\eta^3} + \frac{2}{(\eta+\xi)^2}\frac{df}{d\eta}\frac{d^3f}{d\eta^3}\right], \\ - N_5\left[3\left(\frac{d^3f}{d\eta^3}\right)^2 + \frac{2}{(\eta+\xi)^2}\left(\frac{d^2f}{d\eta^2}\right)^2 + \frac{3}{(\eta+\xi)^4}\left(\frac{df}{d\eta}\right)^2\right], \\ + \frac{4N_5}{(\eta+\xi)^3}\frac{df}{d\eta}\frac{d^2f}{d\eta^2} - \frac{\xi}{(\eta+\xi)^3}\left(\frac{n+1}{2}\right)f\frac{df}{d\eta} - \frac{H_0^2\xi^2}{(\eta+\xi)^2}\left(\frac{d^2f}{d\eta^2} - \frac{1}{\eta+\xi}\frac{df}{d\eta}\right), \\ = 0, \end{aligned} \tag{21}$$

subject to

$$f(\eta)|_{\eta=0} = 0, \frac{df}{d\eta}|_{\eta=0} = 1, \frac{df}{d\eta}|_{\eta=\infty} = 0, \frac{d^2f}{d\eta^2}|_{\eta=\infty} = 0, \tag{22}$$

where $N_5 = m\beta_0\left(\frac{d^2f}{d\eta^2} - \frac{1}{\eta+\xi}\frac{df}{d\eta}\right)$.

Validating the present model, the second tier over curved stretching mechanism occurs when $\beta_0 = 0$, $H_o = 0$, and $n \geq 1$ give

$$\begin{aligned} \frac{d^4f}{d\eta^4} + \frac{2}{\eta+\xi}\frac{d^3f}{d\eta^3} - \frac{1}{(\eta+\xi)^2}\frac{d^2f}{d\eta^2} + \frac{1}{(\eta+\xi)^3}\frac{df}{d\eta}, \\ + \frac{\xi}{\eta+\xi}\left[\left(\frac{n+1}{2}\right)f\frac{d^3f}{d\eta^3} - \left(\frac{3n-1}{2}\right)\frac{df}{d\eta}\frac{d^2f}{d\eta^2}\right], \\ + \frac{\xi}{(\eta+\xi)^2}\left[\left(\frac{n+1}{2}\right)f\frac{d^2f}{d\eta^2} - \left(\frac{3n-1}{2}\right)\left(\frac{df}{d\eta}\right)^2\right], \\ = \frac{\xi}{(\eta+\xi)^3}\left(\frac{n+1}{2}\right)f\frac{df}{d\eta}. \end{aligned} \tag{23}$$

It is worth mentioning that numerical solutions and homotopy analysis solutions have been presented so far in response to Eq. 23, see ref. [33]

4 Heat transfer analysis

Energy equation incorporating radiation, viscous dissipation, and surface frictional heating can be expressed as

$$\begin{aligned} \rho C_p\left(\frac{DT}{Dt}\right) - \nabla(K_0\nabla T) = & \eta_0\left[\frac{\sinh^{-1}(\alpha\Delta)}{\alpha\Delta}\right]^m(2S_{rr}^2 + 2S_{rs}^2 + 2S_{ss}^2), \\ & - \partial_r Q_0 - \frac{\sigma B_0^2 R^2}{(r+R)^2}u^2, \end{aligned} \tag{24}$$

such that $T = T_w$ represents the surface temperature; $T \to T_\infty$, the ambient temperature; K_0, the thermal conductivity of the Sutterby fluid; C_p, the specific heat of the fluid at constant pressure; and Q_0, the heat flux. The last term in Eq. 24 contributes surface frictional heating effect. Taking the curvilinear coordinate expansion, this equation can be expressed as

$$\begin{aligned} v\partial_r T + \frac{Ru}{r+R}\partial_s T = & \frac{K_0}{\rho C_p}\left(\partial_{rr}T + \frac{R\partial_r T}{r+R} + \frac{R^2\partial_{ss}T}{(r+R)^2}\right), \\ & + \frac{\eta_0(S_{rr}^2 + S_{rs}^2 + S_{ss}^2)}{\rho C_p}\left[1 - \frac{m\alpha^2}{6}(2S_{rr}^2 + S_{rs}^2 + 2S_{ss}^2)\right], \\ & - \frac{\partial_r Q_0}{\rho C_p} + \frac{\sigma B_0^2 R^2}{\rho C_p(r+R)^2}u^2, \end{aligned} \tag{25}$$

with the condition specify as

$$PST:\ T = T_w|_{r=0} = 0, T|_{r\to\infty} \to T_\infty, \tag{26}$$

$$PHF:\ -K_0\frac{\partial T}{\partial r}|_{r=0} = B\left(\frac{s}{l}\right)^2, T|_{r\to\infty} \to T_\infty. \tag{27}$$

Imposing the Rosseland approximation for heat flux,

$$Q_0 = \frac{4\sigma^\star}{3k^\star}\frac{\partial T^4}{\partial r}, \tag{28}$$

but the linear radiative flux in Eq. 28 about T_∞ gives

$$\frac{\partial Q_0}{\partial_r} = -\frac{\partial}{\partial r}\left(\frac{4\sigma^\star}{3k^\star}\partial_r\left[4T_\infty^3 T - 3T_\infty^4\right]\right). \tag{29}$$

Using Eq. 29 in Eq. 25, one can get

$$\begin{aligned} &v\partial_r T + \frac{Ru}{r+R}\partial_s T = \frac{K_0}{\rho C_p}\left(1 + \frac{16\sigma^\star T_\infty^2}{3k^\star K_0}\right)\partial_{rr}T + \frac{K_0}{\rho C_p}\left(\frac{\partial_r T}{r+R} + \frac{R^2\partial_{ss}T}{(r+R)^2}\right),\\ &+\frac{\eta_0}{\rho C_p}\left(\partial_r u - \frac{u}{r+R}\right)^2\left[1 - \frac{m\alpha^2}{6}\left(\partial_r u - \frac{u}{r+R}\right)^2\right],\\ &+\frac{\sigma B_0^2 R^2}{\rho C_p (r+R)^2}u^2. \end{aligned} \tag{30}$$

Define similarity transitions of the form

$$PST:\ \theta(\eta) = \frac{T - T_\infty}{T_w - T_\infty}, \tag{31}$$

$$PHF:\ -K_0(T - T_\infty) = D\left(\frac{s}{l}\right)^2\sqrt{\frac{\nu}{bs^{n+1}}}\theta(\eta). \tag{32}$$

Applying Eqs 15-17 and Eqs 31, 32 in Eq. 25, one can get

$$\begin{aligned} (1+Rd)\frac{d^2\theta}{d\eta^2} + \frac{1}{\eta+\xi}\frac{d\theta}{d\eta} + \frac{\mathrm{Pr}\xi}{\eta+\xi}\left[\left(\frac{n+1}{2}\right)f\frac{d\theta}{d\eta} + \eta\left(\frac{n-1}{2}\right)\frac{d\theta}{d\eta}\frac{df}{d\eta}\right],\\ + Br\left(\frac{d^2 f}{d\eta^2} - \frac{1}{\eta+\xi}\frac{df}{d\eta}\right)^2\left[1 - m\beta_0\left(\frac{d^2 f}{d\eta^2} - \frac{1}{\eta+\xi}\frac{df}{d\eta}\right)^2\right],\\ = -\frac{\tau\xi^2}{(\eta+\xi)^2}\left(\frac{df}{d\eta}\right)^2, \end{aligned} \tag{33}$$

where $\mathrm{Pr} = \frac{\eta_0 C_p}{K_0}$ is the Prandtl number, $Ec = \frac{u_w^2}{C_p(T_w - T_\infty)}$ the Eckert number, $Rd = \frac{16\sigma^\star T_\infty^3}{3k^\star K_0}$ the radiation parameter, $\tau = \frac{\sigma u B_0^2 U_\infty^2}{n\rho C_p(T_w - T_\infty)}$ the frictional heating parameter, and $Br = PrEc$ the Brinkman number. It should be noted that, for PHF analysis, $\theta(\eta)$ becomes $\vartheta(\eta)$ in Eq. 33.

The corresponding boundary conditions become

$$PST:\ \theta(0)|_{\eta=0} = 1, \theta(\infty)|_{\eta=\infty} = 0, \tag{34}$$

$$PHF:\ \frac{d\vartheta(0)}{d\eta}|_{\eta=0} = -1, \vartheta(\infty)|_{\eta=\infty} = 0. \tag{35}$$

In view of engineering and industrial interest, the physical quantities, such as skin friction coefficient C_f, Nusselt number Nu, and local Nusselt $Nu^\star$, are calculated as follows:

$$C_f = \frac{\tau_{rs}|_{r=0}}{\frac{1}{2}\rho u_w^2}, Nu = \frac{sQ_0}{K_0(T - T_w)}, Nu^\star = \frac{sQ_0}{D\left(\frac{s}{l}\right)^2}, \tag{36}$$

using $\tau_{rs} = \eta_0 \mathbf{A_1}\left[\frac{\sinh^{-1}(\alpha\Delta)}{\alpha\Delta}\right]^m\left(\partial_r u - \frac{u}{r+R}\right)|_{r=0}$, $Q_0 = -K_0\partial_r T|_{r=0}$, and $u_w = bs^n$,and these yield

$$-R_{es}^{\frac{1}{2}}C_f = \left(\frac{d^2 f(0)}{d\eta^2} - \frac{1}{\xi}\right)\left[1 - \beta_0\left(\frac{d^2 f(0)}{d\eta^2} - \frac{1}{\xi}\right)^2\right], \tag{37}$$

$$R_{es}^{-\frac{1}{2}}Nu = -\frac{d\theta(0)}{d\eta}, R_{es}^{-\frac{1}{2}}Nu^\star = \vartheta(0). \tag{38}$$

Eq. 38 gives the surface rate of the heat transfer for PST and PHF, respectively.

5 Numerical computations

The numerical technique to solve the higher order nonlinear coupled differential Eqs 21, 33 subjected to Eqs 22, 34, 35 is considered in this section. Initialize the boundary value problem (BVP) into the initial value problem (IVP) using the variables

$$\left(f, \frac{df}{d\eta}, \frac{d^2 f}{d\eta^2}, \frac{d^3 f}{d\eta^3}, \theta, \frac{d\theta}{d\eta}, \vartheta, \frac{d\vartheta}{d\eta}\right)^T = (y, y_1, y_2, y_3, y_4, y_5)^T. \tag{39}$$

Linearizing into the system of first-order equations can be expressed as

$$\begin{pmatrix} y' \\ y_1' \\ y_2' \\ y_3' \\ y_4' \\ y_5' \end{pmatrix} = \begin{pmatrix} y_1 \\ y_2 \\ y_3 \\ -2\lambda y_3 + \lambda^2 y_2 - \lambda^3 y_1 - \lambda\xi\left[\left(\frac{m+1}{2}\right)y y_3 - \left(\frac{3m-1}{2}\right)y_1 y_2\right] \\ +\xi\lambda^3\left(\frac{m+1}{2}\right)y y_2 - \lambda^2\xi\left[\left(\frac{m+1}{2}\right)y y_2 - \left(\frac{3m-1}{2}\right)y_1^2\right] \\ +m\beta(y_2 - \lambda y_1)(3y_2 y_3' + 3\lambda y_1 y_3' - 2\lambda y_2 y_3 + 2\lambda^2 y_1 y_3 + 2\lambda^3 y_3^2) \\ +m\beta(y_2 - \lambda y_1)3\lambda^4 y_2^2 + 3y_3^2 - 4\lambda^3 y_1 y_2 - H_0^2 y^2\xi^2(y_2 - \lambda y_1) \\ y_5 \\ -\frac{1}{1+Rd}\left(\lambda y_6 + \lambda\xi\mathrm{Pr}\left[\left(\frac{m+1}{2}\right)y y_5 + \eta\left(\frac{m-1}{2}\right)y_1 y_5\right] + \tau\xi^2\lambda^2 y_1^2\right) \\ -\frac{Br}{1+Rd}(y_2 - \lambda y_1)^2[1 - \beta(y_2 - \lambda y_1)] \end{pmatrix}, \tag{40}$$

subject to the boundary conditions

$$\begin{pmatrix} y_1(0) \\ y_2(0) \\ y_3(0) \\ y_4(0) \\ y_5(0) \\ y_6(0) \end{pmatrix} = \begin{pmatrix} 0 \\ 1 \\ c_1 \\ c_2 \\ 1 \\ c_3 \end{pmatrix}, \tag{41}$$

where $\lambda = \frac{1}{\eta+\xi}$ and c_1, c_2, and c_3 are missing initial conditions. It is worth noting that θ and ϑ are interchanged to obtain the solution of the PHF case.

Implementing the standard Keller–Box shooting method and the Jacobi iterative technique [18], let

$$w' = w_1, w_1' = w_2, w_2' = w_3, \ldots, w_{n-1}' = H(\xi, w_1, w_2, w_3, \ldots, w_{n-1}), \tag{42}$$

$$\begin{aligned} \frac{w_i^{n+1} - w_{i-1}^n}{\delta h} &= (w_1)_{i-1/2}^n,\\ \frac{(w_1)_i^{n+1} - (w_1)_{i-1}^n}{\delta h} &= (w_2)_{i-1/2}^n,\\ &\ldots,\\ \frac{(w_{n-1})_i^{n+1} - (w_{n-1})_{i-1}^n}{\delta h} &= H_2\left(\xi_{i-1/2}^n, w_{i-1/2}^n, (w_1)_{i-1/2}^n, \ldots, (w_{n-1})_{i-1/2}^n\right). \end{aligned} \tag{43}$$

Equation 43 is explicitly implemented into Eq. 40 subject to conditions Eq. 41 as follows:

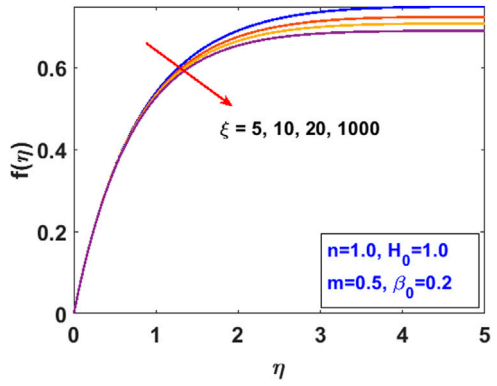

FIGURE 2
Effects of ξ on $f(\eta)$.

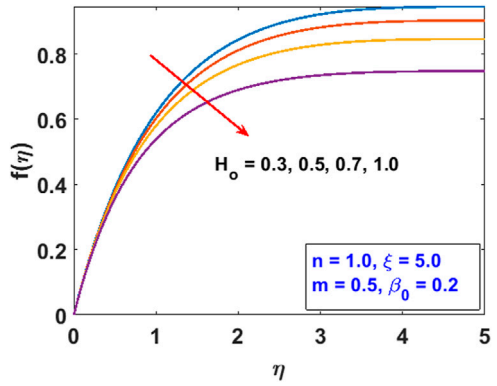

FIGURE 3
Effects of H_o on $f(\eta)$.

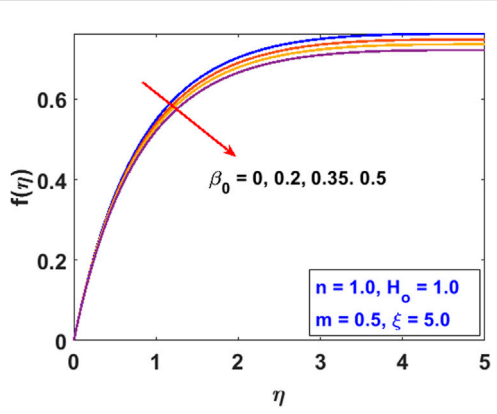

FIGURE 4
Effects of β_0 on $f(\eta)$.

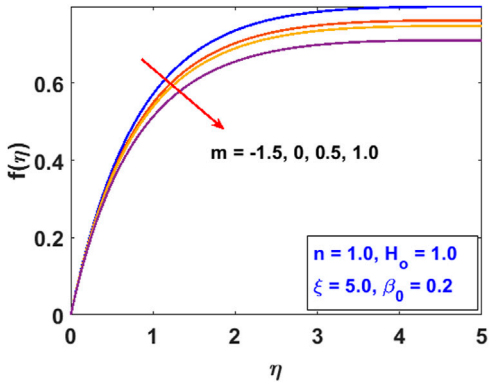

FIGURE 5
Effects of m on $f(\eta)$.

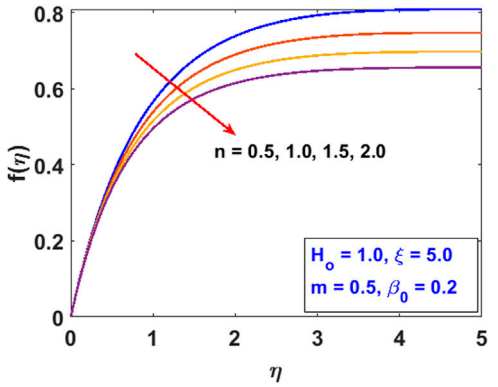

FIGURE 6
Effects of n on $f(\eta)$.

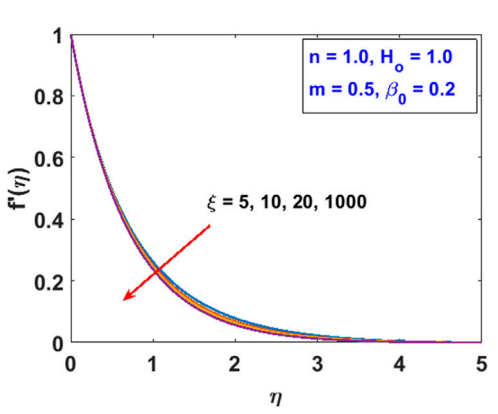

FIGURE 7
Effects of ξ on $f'(\eta)$.

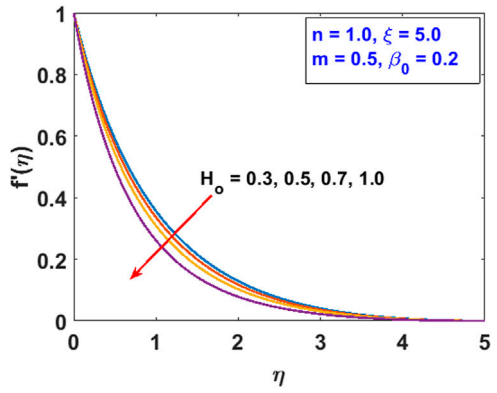

FIGURE 8
Effects of H_o on $f'(\eta)$.

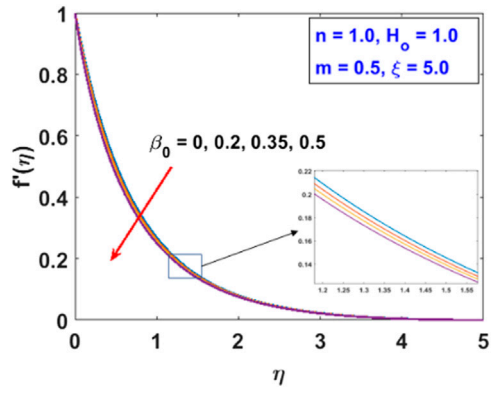

FIGURE 9
Effects of β_0 on $f'(\eta)$.

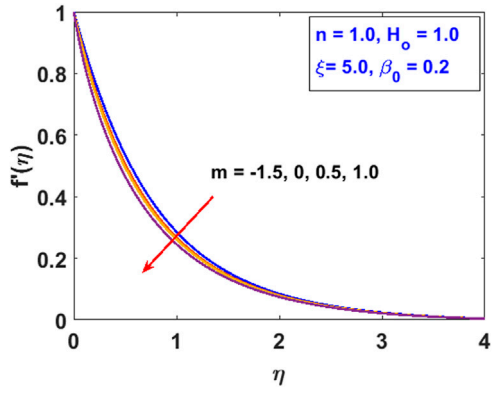

FIGURE 10
Effects of m on $f'(\eta)$.

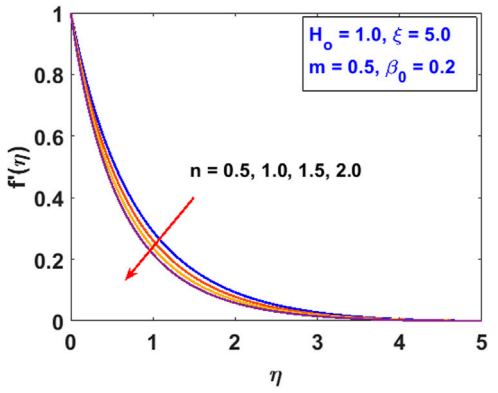

FIGURE 11
Effects of n on $f'(\eta)$.

$$\frac{y_i^{n+1} - y_{i-1}^{n}}{\delta h} + \frac{(y_1)_i^n + (y_1)_{i-1}^n}{2} = 0, \tag{44}$$

$$y_0^{n+1} = 0, \tag{45}$$

$$\frac{(y_1)_i^{n+1} - (y_1)_{i-1}^n}{\delta h} + \frac{(y_2)_i^n + (y_2)_{i-1}^n}{2} = 0, \tag{46}$$

$$(y_1)_0^{n+1} = 1, \tag{47}$$

$$\frac{(y_2)_i^{n+1} - (y_2)_{i-1}^n}{\delta h} + \frac{(y_3)_i^n + (y_3)_{i-1}^n}{2} = 0, \tag{48}$$

$$(y_2)_0^{n+1} = c_1, \tag{49}$$

$$\begin{aligned}\frac{(y_3)_i^{n+1}}{\delta h} = {} & \frac{(y_3)_{i-1}^n}{\delta h} - \frac{(y_3)_i + (y_3)_{i-1}}{\eta+\xi} - \frac{N_5\left((y_1)_i + (y_1)_{i-1}\right)\left((y_2)_i + (y_2)_{i-1}\right)}{(\eta+\xi)^3} \\ & - \frac{(n+1)(y_i + y_{i-1})\left((y_3)_i + (y_3)_{i-1}\right)\xi}{8(\eta+\xi)} - \frac{(y_1)_i + (y_1)_{i-1}}{2(\eta+\xi)^3} \\ & + \frac{(3n-1)\left((y_1)_i + (y_1)_{i-1}\right)\left((y_2)_i + (y_2)_{i-1}\right)\xi}{8(\eta+\xi)} + \frac{(y_2)_i + (y_2)_{i-1}}{2(\eta+\xi)^2} \\ & - \frac{(n+1)(y_i + y_{i-1})\left((y_2)_i + (y_2)_{i-1}\right)\xi}{8(\eta+\xi)^2} + \frac{(3n-1)\left((y_1)_i + (y_1)_{i-1}\right)^2\xi}{8(\eta+\xi)^2} \\ & + \frac{(n+1)(y_i + y_{i-1})\left((y_1)_i + (y_1)_{i-1}\right)\xi}{8(\eta+\xi)^3} + \frac{H_0^2\xi^2(y_2)_i + (y_2)_{i-1}}{2(\eta+\xi)^2} \\ & + \frac{3N_5\left((y_2)_i + (y_2)_{i-1}\right)\left((y_3)_i^{n+1} - (y_3)_{i-1}^n\right)}{4\delta h} + \frac{3N_5\left((y_3)_i + (y_3)_{i-1}\right)^2}{4} \\ & - \frac{3N_5\left((y_1)_i + (y_1)_{i-1}\right)\left((y_3)_i^{n+1} - (y_3)_{i-1}^n\right)}{4\delta h(\eta+\xi)} + \frac{N_5\left((y_2)_i + (y_2)_{i-1}\right)^2}{2(\eta+\xi)^2} \\ & - \frac{N_5\left((y_2)_i + (y_2)_{i-1}\right)\left((y_3)_i + (y_3)_{i-1}\right)}{2(\eta+\xi)} + \frac{3N_5\left((y_1)_i + (y_1)_{i-1}\right)^2}{4(\eta+\xi)^4} \\ & + \frac{N_5\left((y_1)_i + (y_1)_{i-1}\right)\left((y_3)_i + (y_3)_{i-1}\right)}{2(\eta+\xi)^2} - \frac{H_0^2\xi^2(y_1)_i + (y_1)_{i-1}}{2(\eta+\xi)^3},\end{aligned} \tag{50}$$

$$(y_3)_0^{n+1} = c_2, \tag{51}$$

$$\frac{(y_4)_i^{n+1} - (y_4)_{i-1}^n}{\delta h} + \frac{\left((y_5)_1\right)_i^n + \left((y_5)_1\right)_{i-1}^n}{2} = 0, \tag{52}$$

$$(y_4)_0^{n+1} = 1, \tag{53}$$

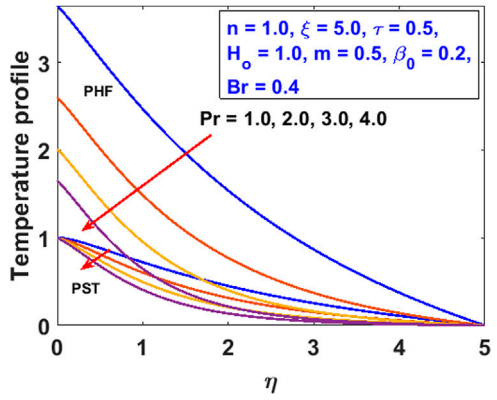

FIGURE 12
Effects of *Pr* on temperature.

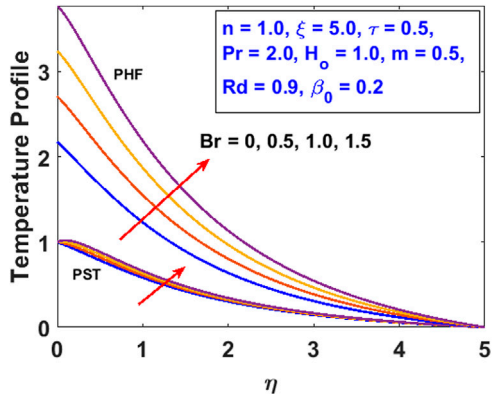

FIGURE 13
Effects of *Br* on temperature.

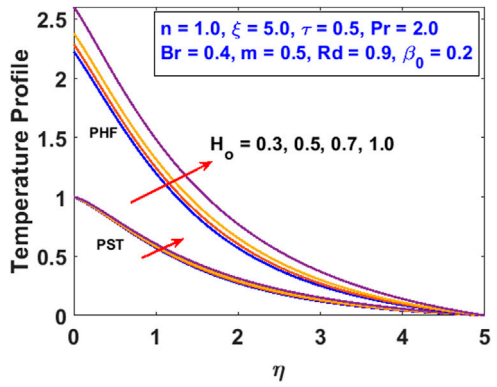

FIGURE 14
Effects of H_o on temperature.

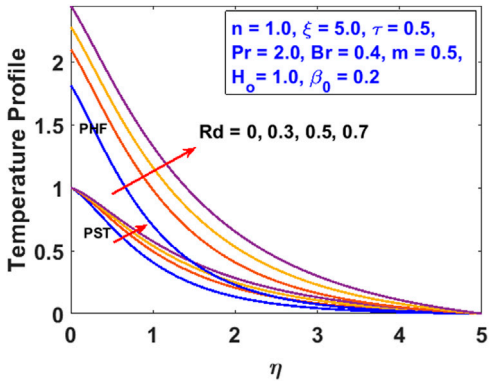

FIGURE 15
Effects of *Rd* on temperature.

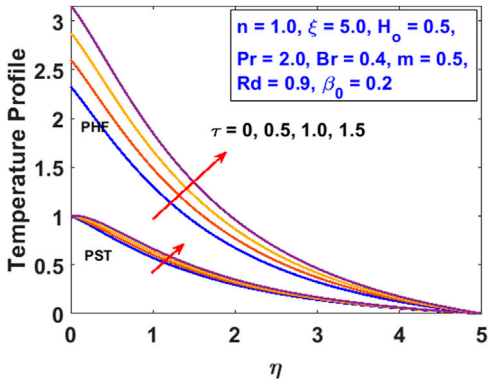

FIGURE 16
Effects of τ on temperature.

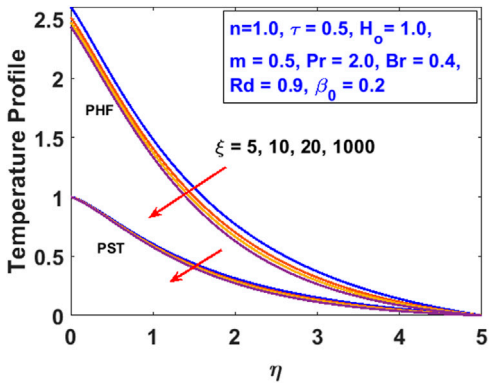

FIGURE 17
Effects of ξ on temperature.

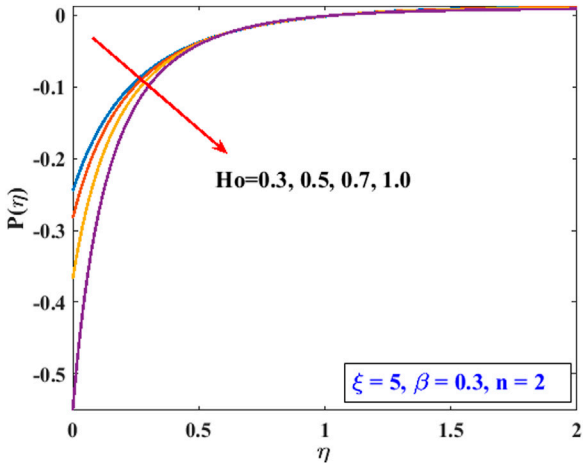

FIGURE 18
Effects of H_o on $P(\eta)$.

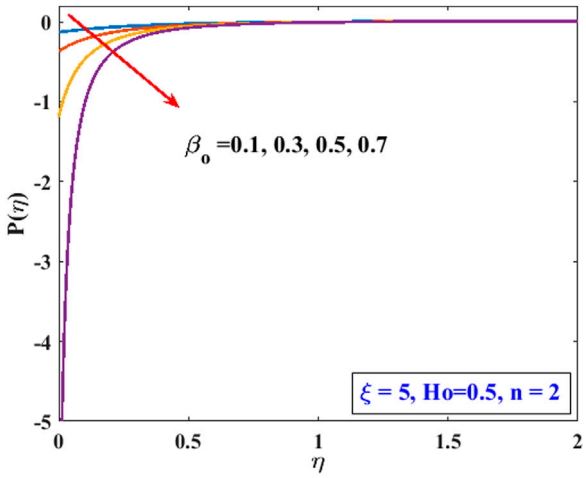

FIGURE 20
Effects of β_0 on $P(\eta)$.

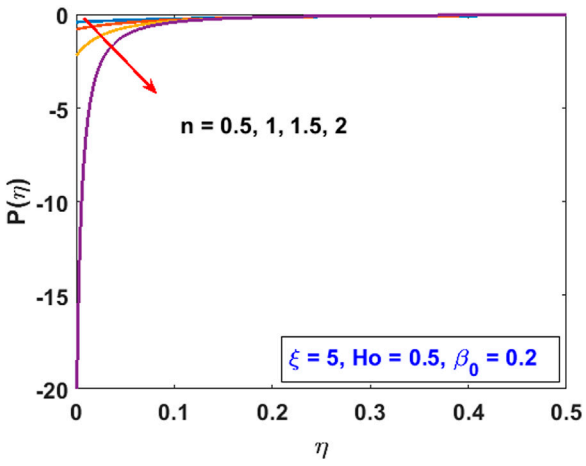

FIGURE 19
Effects of n on $P(\eta)$.

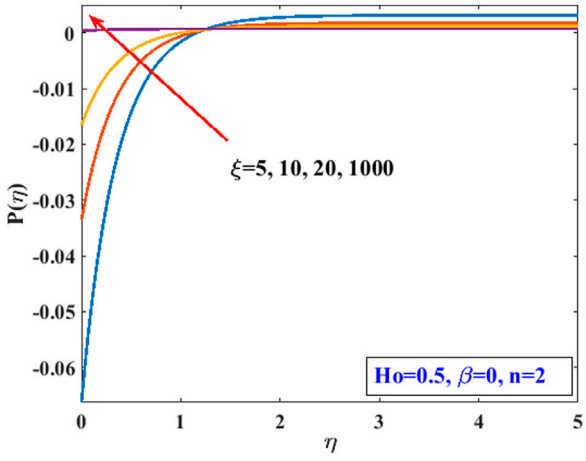

FIGURE 21
Effects of ξ on $P(\eta)$.

$$\frac{(y_5)_i^{n+1} - (y_5)_{i-1}^{n}}{\delta h} = -\frac{(y_5)_i + (y_5)_{i-1}}{2(1+Rd)(\eta+\xi)} - \frac{\tau\xi^2\left((y_1)_i + (y_1)_{i-1}\right)}{2(\eta+\xi)^2} - \frac{(n+1)(y_i + y_{i-1})\left((y_5)_i + (y_5)_{i-1}\right)\mathrm{Pr}\xi}{8(\eta+\xi)} - \frac{\eta(n-1)\left((y_1)_i + (y_1)_{i-1}\right)\left((y_5)_i + (y_5)_{i-1}\right)\mathrm{Pr}\xi}{8(\eta+\xi)} - \frac{BrN_5^2}{m^2\beta^2} + \frac{BrN_5^4}{m^3\beta^3}, \tag{54}$$

$$(y_5)_0^{n+1} = c_3, \tag{55}$$

where c_1, c_2, and c_3 are initial guesses obtained through MATLAB fsolve. The accuracy of the initial guesses is checked against endpoint $\eta_{\max}$. Otherwise, the values are updated, and iterations continue. A step size, $\delta h = 10^{-2}$, is used until the solution is obtained, which satisfies the endpoint initially at infinity and is subject to the stopping criterion given as

$$|\|w^{(n+1)}\|_2 - \|w^n\|_2| < \epsilon, \tag{56}$$

such that ϵ remains the fixed tolerance value of 10^{-8} to ascertain the numerical results. The algorithm is implemented through the ode45 built-in MATLAB command.

6 Results and graphical analysis

The behaviors of the field quantities, velocity, and temperature against various flow parameters are presented in this section. Fluid parameters characterized in this problem include the radius of curvature, ξ, magnetic parameter, H_o, Sutterby fluid parameters

TABLE 1 Comparison of numerical results $\xi \to \infty$ with published results.

	Hammad [9]	G and S [12]	Khan et al. [29]	Ijaz et al. [30]	Result
$-\frac{d^2 f(0)}{d\xi^2}$	-	-	1.000000	1.000000	1.000001
Pr	$-\frac{d\theta(0)}{d\xi}$	$-\frac{d\theta(0)}{d\xi}$	$-\frac{d\theta(0)}{d\xi}$	$-\frac{d\theta(0)}{d\xi}$	Result
0.07	0.065600	0.065600	0.035526	0.130816	0.130810
0.2	0.139100	0.139100	0.164037	0.196550	0.196552
0.7	0.453900	0.453900	0.418299	0.454446	0.454448
20	3.353900	3.353900	3.256030	3.359500	3.353902
70	6.462200	6.462200	6.366620	6.462290	6.462293

TABLE 2 Numerical values of the surface rate of heat transfer for various ξ, β_0, *Ho*, *Pr*, *Br*, *Rd*, and τ when m =0.2.

ξ	β_0	*Ho*	Pr	*Br*	*Rd*	τ	$-\frac{d^2 f(0)}{d\xi^2}$	PST $\left(-\frac{d\theta(0)}{d\xi}\right)$	PHF $\left(-\frac{d\vartheta(0)}{d\xi}\right)$
5	0.1	-	2.0	0.4	0.9	0.5	1.12841	0.27076	2.28220
-	0.2	-	-	-	-	-	1.13894	0.27135	2.28272
-	0.3	-	-	-	-	-	1.14994	0.27193	2.28326
-	0.4	-	-	-	-	-	1.16146	0.27251	2.28385
-	0.3	0	-	-	-	-	1.03011	0.30275	2.19509
-	-	0.3	-	-	-	-	1.07421	0.29209	2.22596
-	-	0.5	-	-	-	-	1.14994	0.27193	2.28326
-	-	0.7	-	-	-	-	1.25793	0.23908	2.37471
10	-	0.5	1.0	-	-	-	1.14148	0.11253	3.26471
-	-	-	1.5	-	-	-	-	0.20778	2.64037
-	-	-	2.0	-	-	-	-	0.30261	2.21633
-	-	-	2.5	-	-	-	-	0.39434	1.91669
-	-	-	2.0	0	-	-	-	0.39243	2.05967
-	-	-	-	0.5	-	-	-	0.28016	2.25549
-	-	-	-	1.0	-	-	-	0.16788	2.45131
-	-	-	-	1.5	-	-	-	0.05560	2.64713
20	-	-	-	0.4	0.3	-	1.14257	0.45791	1.72664
-	-	-	-	-	0.5	-	-	0.39987	1.88689
-	-	-	-	-	0.7	-	-	0.35346	2.04021
-	-	-	-	-	0.9	-	-	0.31571	2.18627
-	-	-	-	-	0.9	0.1	-	0.46263	1.93157
-	-	-	-	-	-	0.2	-	0.42590	1.99525
-	-	-	-	-	-	0.3	-	0.38917	2.05892
-	-	-	-	-	-	0.4	-	0.35244	2.12260

m and β_0, and stretching power index n. The behavior of temperature distribution is examined against Prandtl number *Pr*, Brinkman number *Br*, magnetic parameter H_o, radiation parameter *Rd*, and surface frictional heating parameter τ. Flow stream function is plotted in Figures 2–6 against the radius of curvature, Lorentz force, Sutterby fluid parameters, and stretching power index,

respectively. In these graphs, the enhancement of any flow parameter decreases the flow trajectories. Physically, this can be seen as a means of controlling the flow field and boundary-layer region. Figures 7, 8 show that the velocity decreases for increasing ξ and H_o and consequently reduces the boundary-layer thickness. Thus, the flow field and flow trajectories can be significantly controlled *via* the size of these parameters. The impacts of Sutterby fluid parameters, β_0 and m, on the velocity profile are shown in Figures 9, 10, respectively. The graphs infer that velocity profiles decrease for optimizing the fluid parameters. Physically, this observation shows that increasing fluid parameters enhances the viscous resistance (shear-thickening) property of the fluid and invariably controls the flow velocity and associated boundary-layer thickness.

Figure 11 explains the effect of stretching power n on the velocity distribution. The graph shows a decrease in velocity for large n. Thus, it confirms that nonlinear stretching velocity for the boundary-driven flow could serve as a means of controlling the flow field. This observation is significant and can play a vital role in flow past stretchable materials. The effect of thermal kinetics parameters Pr, Br, H_o, Rn, τ, and ξ on both PST, $\theta(\eta)$, and PHF, $\vartheta(\eta)$ scenarios are presented in Figures 12–17. Figure 12 shows the impact of the Prandtl number Pr on the temperature distribution, revealing that the temperature region with the thermal boundary-layer thickness decay significantly. In other words, it is caused by the increased thermal conductivity of the Sutterby fluid. Furthermore, this observation is prominently seen in PHF, meaning that heat flow can be enhanced by virtue of the prescribed heat flux than surface temperature. Figure 13 elucidates the effect of the Brinkman number Br on the temperature distribution. In this graph, the temperature region is expanded by increasing Br in the PST and PHF cases. However, it infers that large Br weakens the fluid's viscous bond and generates additional heat from the fluid. Furthermore, it is noted that the heat occurrence is more intense in the PHF than in the PST region. An increase in the temperature distribution and the thermal boundary-layer thickness for higher magnetic number H_o is witnessed in Figure 14. The reason is that quantum heat is produced as the flow velocity is disrupted by the opposing large Lorentz force and then enlarges the temperature region. Figure 15 presents an optimizing effect of increasing the radiation parameter Rd on the temperature profile. This observation agrees with the usual and existing fact that radiation serves as an additional source of heat generation. Thus, the increase is more rapid for the PHF scenario compared to the PST region. Increasing the surface frictional heating parameter, τ optimizes the temperature profile in both heat situations, as shown in Figure 16. This impact is caused by surface induction and adding more heat from the solid surface to the fluid. However, a further effect is displayed in the PHF than in the PST profile. The impact of the dimensionless radius of curvature on the temperature profile is given in Figure 17. The temperature distribution with associated thermal boundary-layer thickness is enhanced to increase the curvature (reducing the radius of curvature). This observation concludes that heat travels faster over a curved surface compared to a flat surface and is more profound in the PHF than in the PST cases. It shows an important result and a substantial contribution to this study.

The behavior of pressure is significant to the flow field over the curved structure; therefore, pressure variations need to be discussed. Figures 18–21 depict the pressure variations due to the Lorentz force, stretching the power index, Sutterby fluid parameter, and radius of curvature. Clearly, Figure 18 elucidates a diminished pressure profile for a large Lorentz force. This observation confirms the earlier behavior of flow trajectory and velocity field (see Figures 3, 8). The gradual decrease in pressure profiles is shown in Figures 18–21. These observations support the graphs in Figures 8, 9, 11 and further accentuate flow behaviors over the curved stretching mechanism. In other words, fluid flow can be regulated and controlled by means of the stretching power index. Likewise, Figure 20 elucidates a slight decrease in the flow pressure for a large fluid parameter, which shows a powerful influence of the fluid parameter for regulating flow velocity. It further substantiates the observations made in Figures 4, 9. Figure 21 is plotted to authenticate the present model; see Eq. 21. In validation of the present investigation, we set the pressure to zero, $P(\eta) = 0$ and the large dimensionless radius of curvature, $\xi \to \infty$ (surface becomes flat). A valuable known result for fluid flow over the flat stretching surface is achieved [23–25]. Table 1 shows an excellent agreement of the computational values for surface drags compared to the published studies. Table 2 is provided in the remark of the surface rate of heat transfer for the PST and PHF cases. It also presents the impact of the magnetic field on skin friction coefficient and rate of heat transfer for PST and PHF cases.

7 Concluding remark

The magnetohydrodynamic flow of the non-Newtonian Sutterby fluid driven by nonlinear power-law velocity over a continuous stretching curved mechanism has been addressed. The analysis is presented in a radially varying magnetic field acting perpendicular to the flow direction. Viscous dissipation, surface frictional heating, and radiation serve as the additional source of heat for prescribed surface temperature, PST, and prescribed heat flux, PHF. Governing models are theoretically formulated under desirable physical phenomena to ensure realistic flow behaviors. Computation is performed using the standard Keller–Box method and the Jacobi iterative scheme. The following results were plausibly recorded and summarized.

1. The velocity field decreases to increase Sutterby fluid parameters and stretch the nonlinear power index, whereas the opposite effect occurs to enhance the magnetic field parameter and dimensionless radius of curvature.
2. The temperature distribution increases for large Brinkman number, radiation, and surface frictional heating parameters.
3. Increasing magnetic field generates a large Lorenz force, which enhances the temperature profile.
4. Additional heat is transferred over the curved surface compared to the flat surface, and it is more significant in the PHF than in the PST regions.
5. Heat transfer through the prescribed heat flux is more important to enhance heat flow due to the additional heat generated from the solid surface to the fluid.

6. The results are validated by comparing the surface drags with the published work, authenticating our numerical method and concluding by presenting numerical values for the heat transfer rate in the PST and PHF cases.

Data availability statement

The original contributions presented in the study are included in the article/Supplementary Material. Further inquiries can be directed to the corresponding author.

Author contributions

All authors listed have made a substantial, direct, and intellectual contribution to the work and approved it for publication.

Funding

The research was funded by the University of Oradea, Romania.

Conflict of interest

The authors declare that the research was conducted in the absence of any commercial or financial relationships that could be construed as a potential conflict of interest.

Publisher's note

All claims expressed in this article are solely those of the authors and do not necessarily represent those of their affiliated organizations, or those of the publisher, the editors, and the reviewers. Any product that may be evaluated in this article, or claim that may be made by its manufacturer, is not guaranteed or endorsed by the publisher.

Supplementary material

The Supplementary Material for this article can be found online at: https://www.frontiersin.org/articles/10.3389/fphy.2023.1126003/full#supplementary-material

References

1. Jalil M, Asghar S, Mushtaq M. Analytical solutions of the boundary layer flow of power-law fluid over a power-law stretching surface. *Commun Nonlinear Sci Numer Simulat* (2013) 18:1143–50. doi:10.1016/j.cnsns.2012.09.030

2. Patil VS, Patil NS, Timol MG. A remark on similarity analysis of boundary layer equations of a class of non-Newtonian fluids. *Int J Nonlinear Mech* (2015) 71:127–31. doi:10.1016/j.ijnonlinmec.2014.10.022

3. Anuar NS, Bachok N, Mustafa T, Md Arifin N, Haliza R. Analytical and stability analysis of MHD flow past a nonlinearly deforming vertical surface in Carbon Nanotubes. *A Eng J* (2020) 59(1):497–507. doi:10.1016/j.aej.2020.01.024

4. Kumaran G, Sivaraj R, Reddy AS, Kumar R, Prasad VR. Hydromagnetic forced convective flow of Carreau nanofluid over a wedge plate/stagnation of the plate. *Eur Phys J Spec Top* (2019) 228:2647–59. doi:10.1140/epjst/e2019-900069-2

5. Jalil M, Asghar S. Flow of power-law fluid over a stretching surface: A lie group analysis. *Int J Nonlinear Mech* (2013) 48:65–71. doi:10.1016/j.ijnonlinmec.2012.07.004

6. Wahid NS, Md Arifin N, Turkyilmazoglu M, Hafidz MEH, Abd Rahmin NA. MHD hybrid Cu-Al₂O₃/water nanofluid flow with thermal radiation and partial slip past a permeable stretching surface: Analytical solution. *J Nano Res* (2020) 64:75–91. doi:10.4028/www.scientific.net/jnanor.64.75

7. Hamad AA. Analytical solution of natural convection flow of a nanofluid over a linearly stretching sheet in the presence of magnetic field. *Int Commun Heat Mass* (2011) 38:487–92. doi:10.1016/j.icheatmasstransfer.2010.12.042

8. Gorla RS, Sidawi I. Free convection on a vertical stretching surface with suction and blowing. *Appl Sci Res* (1994) 52:247–57. doi:10.1007/bf00853952

9. Mustaq A, Mustafa M, Hayat T, Alsaedi A Effect of thermal Radiation on the stagnation-point flow of upper-convected Maxwell fluid over a stretching sheet. *J Aerosp Eng*, 27(4), 1–6. (2014). doi:10.1061/(ASCE)AS.1943-5525.0000361

10. Jawadi A, Boutyour H, Cadou JM. Asymptotic numerical method for steady flow of power-law fluids. *J Non-newton Fluid Mech* (2013) 202:22–31. doi:10.1016/j.jnnfm.2013.09.005

11. Zierep J, Fetecau C. Energetic balance for the Rayleigh-Stokes problem of a Maxwell fluid. *Int J Eng Sci* (2007) 45:617–27. doi:10.1016/j.ijengsci.2007.04.015

12. Hayat T, Ijaz MK, Tamoor M, Waqas M, Alsaedi A. Numerical Simulation of heat transfer in MHD Stagnation point flow of Cross fluid model towards a stretched surface. *Results Phys* (2017) 7:1824–7. doi:10.1016/j.rinp.2017.05.022

13. Ijaz MK, Waqas W, Hayat T, Alsaedi A. Magneto-hydrodynamical numerical simulation of heat transfer in MHD stagnation point flow of Cross fluid model towards a stretched surface. *Phys Chem Liq* (2017) 56(5):584–95. doi:10.1080/00319104.2017.1367791

14. Manzur M, Khan M, Rahman M. Mixed convection heat transfer to Cross fluid with thermal radiation: Effects of buoyancy assisting and opposing flows. *Int J Mech Sci* (2018) 138-139:515–23. doi:10.1016/j.ijmecsci.2018.02.010

15. Khan M, Manzur M, Rahman M. On axisymmetric flow and heat transfer of Cross fluid over a radially stretching sheet. *Results Phys* (2017) 7:3767–72. doi:10.1016/j.rinp.2017.08.039

16. Zheng LC, Wang KN, Gao YT. Unsteady flow and heat transfer of a generalized Maxwell fluid due to a hyperbolic sine accelerating plate. *Comp Math Appl* (2011) 61:2209–12. doi:10.1016/j.camwa.2010.09.017

17. Rout BC, Mishra SR. Thermal energy transport on MHD nanofluid flow over a stretching surface: A comparative study. *Eng Sci Tech Int J* (2018) 21(1):60–9. doi:10.1016/j.jestch.2018.02.007

18. Yasir N, Shoaib Arif M. Keller-Box shooting method and its application to nanofluid flow over convectively heated sheet with stability and convergence. *Num Heat Transfer, B: Fundamentals* (2019) 76:152–80. doi:10.1080/10407790.2019.1644924

19. Mohamed R, Eid Kasseb ML, Mohammed T, Sheikholeslami M. Numerical treatment for Carreau nanofluid flow over a porous nonlinear stretching surface. *Results Phys* (2018) 8:1185–93. doi:10.1016/j.rinp.2018.01.070

20. Prasannakumara BC, Gireesha BJ, Krishnamurthy MR, Kumar KG. MHD flow and nonlinear radiative heat transfer of Sisko nanofluid over a nonlinear stretching sheet. *Inf Med Unlocked* (2017) 9:123–32. doi:10.1016/j.imu.2017.07.006

21. Feroz AS, Usman M, Ul Haq R, Wang W. Melting heat transfer analysis of Sisko fluid over a moving surface with nonlinear thermal radiation via collocation method. *Heat Mass Transfer* (2018) 126:1034–42. doi:10.1016/j.ijheatmasstransfer.2018.05.099

22. Lund LA, Omar Z, llyas K. Analysis of dual solution for MHD flow of Williamson fluid with Slippage. *Heliyon* (2019) 5(3):e01345–20. doi:10.1016/j.heliyon.2019.e01345

23. Khalil R, Qaiser A, Malik MY, Ali U. Numerical communication for MHD thermally stratified dual convection flow of Casson fluid yields by stretching cylinder. *Chin J Phys* (2017) 55(4):1605–14. doi:10.1016/j.cjph.2017.05.002

24. Sutterby JL. Laminar converging flow of dilute polymer solutions in conical sections: Part I. Viscosity data, new viscosity model, tube flow solution. *A Ch E J* (1965) 12(1):63–8. doi:10.1002/aic.690120114

25. Gangadhar K, Kannan T, Narasimharao NSIV, Kumar BR, Sakthivel G. Thermo diffusion effects on MHD Casson fluid flow over non-flatness stretching surface: Keller Box method. *Int J Amb Energ* (2021) 42(4):374–82. doi:10.1080/01430750.2018.1531263

26. Batra RL, Eissa M. Helical flow of a sutterby model fluid. *Polym-plast Technol Eng* (1994) 33(4):489–501. doi:10.1080/03602559408010743

27. Hayat T, Sidra A, Ijaz MK, Alsaedi A. Irreversibility aspect to flow of sutterby fluid subject to nonlinear heat flux and Ohmic heating. *App Nanosci* (2019) 9:1215–26. doi:10.1007/s13204-019-01015-3

28. Azhar E, Iqbal Z, Ijaz S, Maraj EN. Numerical approach for stagnation point flow of sutterby fluid impinging to Cattaneo-Christov heat flux model. *Pramana J Phys* (2018) 91:61. doi:10.1007/s12043-018-1640-z

29. Hayat T, Ahmad S, Ijaz MK, Alsaedi A. Modeling chemically reactive flow of sutterby nanofluid by a rotating disk in presence of heat generation/absorption. *Commun Theo Phys* (2018) 69:569. doi:10.1088/0253-6102/69/5/569

30. Sher NA. Biomathematical study of sutterby fluid model for blood flow in stenosed arteries. *Int J Biomaths* (2015) 8(6):1550075. doi:10.1142/s1793524515500758

31. Ahmed S, Farooq M, Javed M, Aisha A. Double stratification effects in chemically reactive squeezed sutterby fluid flow with thermal radiation and mixed convection. *Results Phys* (2018) 8:1250–9. doi:10.1016/j.rinp.2018.01.043

32. Abbas Z, Shabbir MS, Ali N. Numerical Study of magnetohydrodynamic pulsatile flow of sutterby fluid through an inclined overlapping arterial stenosis in the presence of periodic body acceleration. *Results Phys* (2018) 9:753–62. doi:10.1016/j.rinp.2018.03.020

33. Sajid M, Ali N, Javed T, Abbas Z. Stretching a curved surface in a viscous fluid. *Chin Phy Lett* (2010) 27:024703. doi:10.1088/0256-307x/27/2/024703

34. Sanni KM, Asghar S, Jalil M, Okechi NF. Flow of viscous fluid along a nonlinearly stretching curved surface. *Results Phys* (2017) 7:1–4. doi:10.1016/j.rinp.2016.11.058

35. Sanni KM, Hussain Q, Asghar S. Heat transfer analysis for non-linear boundary driven flow over a curved stretching sheet with a variable magnetic field. *Front Phys* (2020) 8:113. doi:10.3389/fphy.2020.00113

36. Naveed M, Abbas Z, Sajid M. Hydromagnetic flow over an unsteady curved stretching surfce. *Eng Sci Tech Int J* (2016) 19:841–5. doi:10.1016/j.jestch.2015.11.009

37. Maria I, Hayat T, Alsaedi A, Hobiny A. Homogeneous-heterogeneous reaction in MHD flow due to an unsteady curved stretching surface. *J Mol Liq* (2016) 221:245–53. doi:10.1016/j.molliq.2016.05.060

38. Abbas Z, Naveed M, Sajid M. Hydromagnetic Slip flow of nanofluid over a Curved Surface with heat generation and thermal radiation. *J Mol Liq* (2016) 215:756–62. doi:10.1016/j.molliq.2016.01.012

39. Sanni KM, Asghar S, Saima R, Wu YC. Nonlinear radiative treatment of hydromagnetic non-Newtonian fluid flow induced by nonlinear convective boundary driven curved sheet with dissipations and chemical reaction effects. *Front Phys* (2021) 1–15. doi:10.3389/fphy.2021.670930

40. Hayat T, Sajjad R, Ellahi R, Alsaedi A, Muhammad T. Homogeneous-heterogeneous reaction in MHD flow of micropolar fluid by a curved stretching surface. *J Mol Liq* (2017) 240:209–20. doi:10.1016/j.molliq.2017.05.054

41. Sanni KM, Hussain Q, Asghar S. Flow of magnetohydrodynamic viscous fluid by curved configuration with non-linear boundary driven velocity. *J Taibah Uni Sci* (2021) 15(1):589–98. doi:10.1080/16583655.2021.1991076

42. Sanni M, Hussain Q, Asghar S. Thermal analysis of a hydromagnetic viscoelastic fluid over a continuous curved stretching surface in the presence of radiative heat flux. *Arab J Sci Eng* (2020) 46:1–8. doi:10.1007/s13369-020-04671-8